

# Detection of liquid penetration into a micropillar surface using quartz crystal microbalance

Pengtao Wang<sup>1</sup>, Junwei Su<sup>1</sup>, Mengyan Shen<sup>2</sup>, Marina Ruths<sup>3</sup>, Hongwei Sun<sup>1\*</sup>

<sup>1</sup>Department of Mechanical Engineering, University of Massachusetts Lowell, Lowell, MA 01854, USA

<sup>2</sup>Department of Physics, University of Massachusetts Lowell, Lowell, MA 01854, USA

<sup>3</sup>Department of Chemistry, University of Massachusetts Lowell, Lowell, MA 01854, USA

## Supporting Information

### S1. Contact angle measurement

The contact angle is an angle formed between the liquid/air interface of a liquid droplet and a solid surface, as shown in Figure S1. It is related to the interfacial energy between three phases, and is given by Young's equation

$$\gamma_{SV} = \gamma_{SL} + \gamma_{LV} \cos \theta_0 \quad (\text{S-1})$$

where  $\gamma_{SV}$ ,  $\gamma_{SL}$ , and  $\gamma_{LV}$  represent the interfacial energy of solid/air, solid/liquid, and liquid/air interfaces, respectively.  $\theta_0$  is the static contact angle on a flat surface.

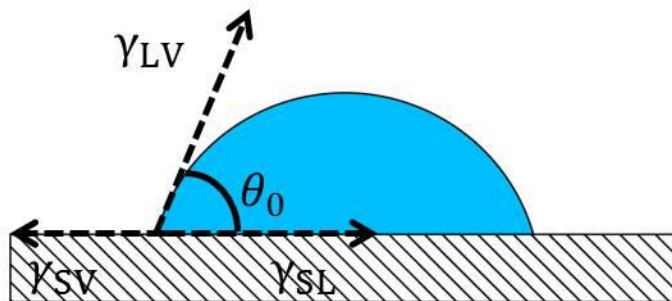


Figure S1. Interfacial energies and contact angle of a water droplet on a flat surface.

For superhydrophobic surfaces with micro-/nanoscale structures/roughness, the contact angle of a droplet in the Cassie state is calculated as

$$\cos \theta_C = f \cos \theta_0 + f - 1 \quad (\text{S-2})$$

In the Wenzel state,

$$\cos \theta_W = R \cos \theta_0 \quad (\text{S-3})$$

where  $\theta_C$  and  $\theta_W$  are contact angles predicted by the Cassie and Wenzel theory, respectively.  $R$  is the roughness factor, which is defined as the ratio of the actual surface area to its horizontal projected surface area, and  $f$  is the fraction of the surface area where liquid is in contact with the solid surface. For the PMMA micropillar-patterned surface,  $R$  and  $f$  can be related to the geometry parameters as

$$R = 1 + \frac{\pi DH}{S^2} \quad (\text{S-4})$$

$$f = \frac{\pi D^2}{S^2} \quad (\text{S-5})$$

where  $D$ ,  $H$  and  $S$  are the diameter, height and center-to-center spacing of the micropillars. In this research, the value of  $f$  is constant at 0.12.

Contact angle measurements were carried out on a drop shape analysis system (DSA 100, KRÜSS GmbH) based on the “Sessile droplet” fitting method. A water droplet of 5  $\mu\text{l}$  was gently loaded on the PMMA micropillar surface and the contact angle was measured immediately after the droplet stopped spontaneously spreading. For comparison, the contact angle of water on a PMMA flat surface was also measured and compared with the reported value in the literature<sup>1</sup>. Table S1 presents the comparison of measured contact angles for flat PMMA surfaces with reported values in literature.

The PFOTS-treated micropillar-patterned surface (pillar height: 24  $\mu\text{m}$ ) had a contact angle of 155.4° ( $\pm 0.8^\circ$ ), as shown in Figure S2. As-imprinted PMMA surface had a contact angle of 107° ( $\pm 0.4^\circ$ ) and the contact angle for plasma treated micropillar-patterned surfaces was around 9.6° ( $\pm 0.2^\circ$ ).

**Table S1. Contact angles for flat PMMA surfaces.**

Surface treatment	Measured	Reported <sup>1</sup>
As-spun PMMA film	$(85.4 \pm 1.0)^\circ$	74 ~ 77°
Hydrophilized	$(41.5 \pm 0.3)^\circ$	40°
Hydrophobized	$(107.3 \pm 0.6)^\circ$	105-112°

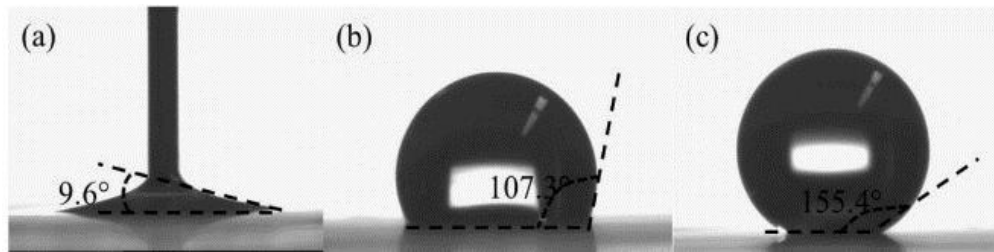


Figure S2. DSA images and contact angle measurements of droplets on (a) superhydrophilic, (b) as-imprinted (unmodified), and (c) superhydrophobic micropillar surfaces.

## **S2. Wenzel and Cassie conditions characterized by cryo FIB-SEM**

This interface morphology was observed by cryo FIB-SEM (Auriga & Carl Zeiss). The hydrophobized pillar surface was first installed on the cryo-stage. Then the samples were submerged into liquid nitrogen after spraying the water droplets onto the surfaces. Therefore, the shape of droplet and interface between liquid and air remain the same by this rapid frozen procedure. After the micro-size droplets were frozen on the surface, the whole set of stage and surface was transported into the chamber of the cryo FIB-SEM via a vacuum transfer system (Leica EM VCT100).

Then the stage was tilted  $53^\circ$  to electron beam, while the ion beam was perpendicular to the sample. With the SEM imaging, a droplet with a diameter of  $103.0 \mu\text{m}$  was selected for the detail analysis (Figure S3(a)). The FIB milling was performed with normal incidence of the ion beam and at ion beam energy of 30 keV, and ion current of

0.48 to 21 nA. Milling of hundreds micrometer droplet required large ion beam currents of 16 nA, resulted in formation of roughness on the milling surface as shown in Figure S3(b). Therefore, an ion beam with low current of 1 nA was applied to polish the milling surface. After the polishing procedure, the frozen liquid-air interface and PMMA pillars are shown in Figure S3 (c).<sup>2</sup> Figure S4 shows the images before and after the polishing.

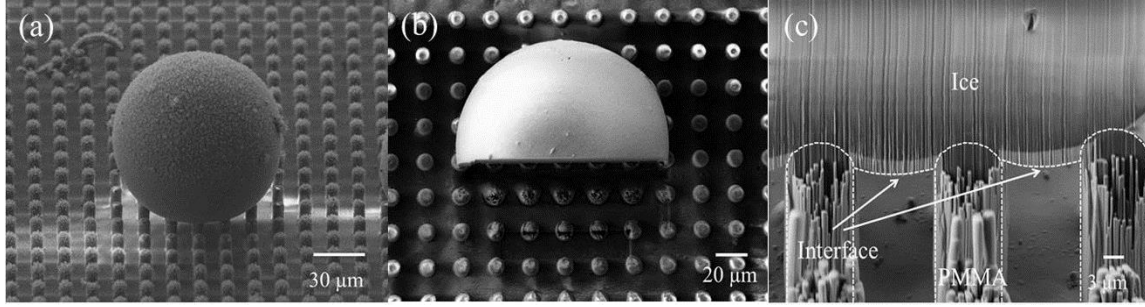


Figure S3. Penetration depth measured with FIB/cryo-SEM. (a) Before FIB milling; (b) After FIB milling; (c) Cross-section of the FIB milled surface, showing the unfilled gaps between the PMMA pillars.

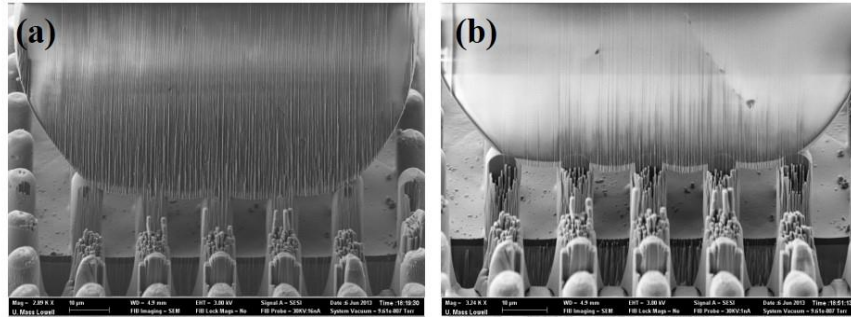


Figure S4. The image of cross-section (a) before and (b) after polishing.

### S3. The meniscus of liquid-air interface

Considering a drop residing on the tops of micropillars, i.e., in the Cassie state, the liquid-air interface underneath the drop experiences a force balance in the vertical direction as described by (Figure. S5)<sup>3</sup>

$$-\sigma(\pi D) \cos(\theta) = \Delta p (S^2 - \pi D^2/4) \quad (\text{S-6})$$

where  $\theta$  is the contact angle of liquid-air interface with micropillars.  $D$  and  $S$  are the diameter and the center-to-center distance of the micropillars, respectively.  $\Delta p$  is the excess pressure (pressure difference between the inside and outside) given by

$$\Delta p = 2\sigma\kappa_d + \rho gh \quad (\text{S-7})$$

where,  $\kappa_d$  and  $h$  are the average curvature and the height of water droplet, respectively.

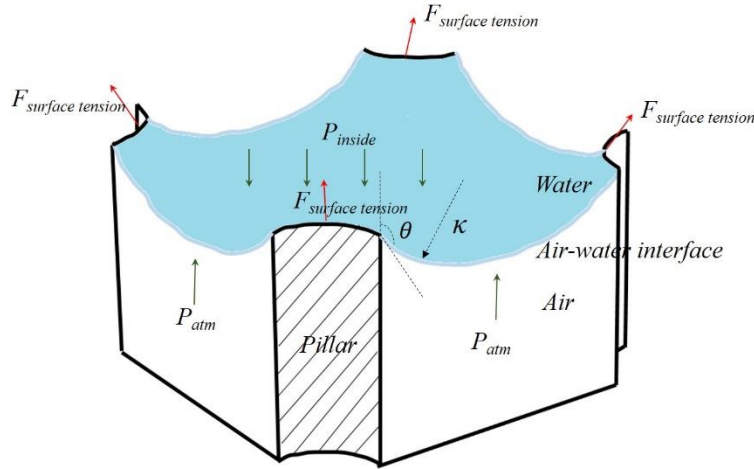


Figure S5. Analysis of the forces acting on the water-air interface underneath a droplet.

Eq. (S-6) can be rewritten as

$$\cos(\theta) = -\frac{\Delta p (S^2 - \pi D^2 / 4)}{\sigma \pi D} \quad (\text{S-8})$$

For the small droplet characterized by cryo FIB-SEM:

Due to the negligible gravity effect, the droplet maintains a spherical shape, as shown in Figure. S3(a). The radius of droplet measured with SEM is  $R_{\text{SEM}} = 51.5 \mu\text{m}$ , and the height is  $h_{\text{SEM}} = 2R_{\text{SEM}} = 103 \mu\text{m}$ . Other parameters are:  $\sigma = 73 \text{ mN/m}$ ,  $\rho = 1000 \text{ kg/m}^3$ ,  $g \approx 10 \text{ N/kg}$  and  $\kappa_{\text{SEM}} = 1/R_{\text{SEM}}$ . The Laplace pressure due to the surface tension is  $2\sigma\kappa_{\text{SEM}} \approx 2,835 \text{ Pa}$ , and the hydrostatic pressure  $\rho gh_{\text{SEM}} \approx 1.0 \text{ Pa}$ , thus the excess pressure is  $\Delta p \approx 2,836 \text{ Pa}$ . For the micropillars used in the cryo FIB SEM, we have  $D_{\text{SEM}} = 8 \mu\text{m}$  and  $S_{\text{SEM}} = 17 \mu\text{m}$ . Therefore, the calculated contact angle of the liquid-air interface with pillar wall is

$$\theta_{SEM} = 111.8^\circ \quad (S-9)$$

which is smaller than the advancing contact angle  $\theta_{adv} = 117^\circ$ .

The meniscus pendant depth ( $\delta$ ) defined as the distance from the contacting point to the lowest point of the meniscus can be calculated as

$$\delta_{SEM} = (L_{SEM}/2)(1 - \sin(\pi - \theta_{SEM}))/\cos(\pi - \theta_{SEM}) = 0.86 \mu m \quad (S-10)$$

The theoretical value is comparable with the measured value of  $0.6 \mu m$ .

For the large drop for the QCM experiment and numerical simulation

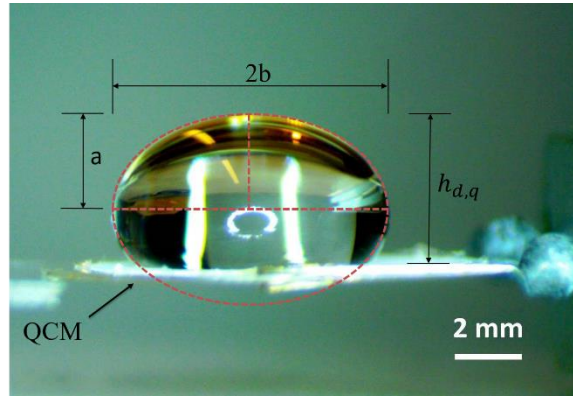


Figure S6. Side-view of water droplet in Cassie state on micropillar-patterned QCM. (pillar diameter =  $10 \mu m$ , spacing =  $15 \mu m$ , height =  $24 \mu m$ )

A simple experiment was conducted to find the contact angle of a large drop as described below: a macro-scale droplet (about  $8 \text{ mm}$  in diameter) was gently deposited on the micropillar-covered surface of a QCM sensor. The water droplet deforms from an initial spherical shape into an oblate spheroid under the effect of gravity as shown in Figure. S6. The major and minor semi-axis  $a$  and  $b$  of the ellipsoidal cross section was measured to be  $a = 2.8 \text{ mm}$ ,  $b = 8.2 \text{ mm}$ , and the drop's height  $h_{QCM} = 4.6 \text{ mm}$ .<sup>4</sup> The Laplace pressure due to surface tension is  $52 \text{ Pa}$  ( $2\sigma\kappa_{QCM} = 52 \text{ Pa}$  with assumption of  $\kappa_{QCM} = 1/a$ ) and the hydrostatic pressure  $\rho gh_{QCM} = 46 \text{ Pa}$ . Having micropillars with diameter  $D_{QCM} = 10 \mu m$  and spacing  $S_{QCM} = 25 \mu m$ , the calculated contact angle is

$$\theta_{QCM} = 91.3^\circ \quad (\text{S-11})$$

The calculated contact angle (a large droplet on superhydrophobic micropillar surface) is in good agreement with the experimental observation using a confocal microscope by Haimov et. al.<sup>5</sup>, who reported that the local mean curvature of the water-air interface is constant and close to zero.

#### S4. Typical responses of micropillar-patterned QCMs

Figure S7 shows the admittance responses of QCM devices with micropillar height of 24  $\mu\text{m}$  when the pillars operate in air, Cassie state, and Wenzel state.

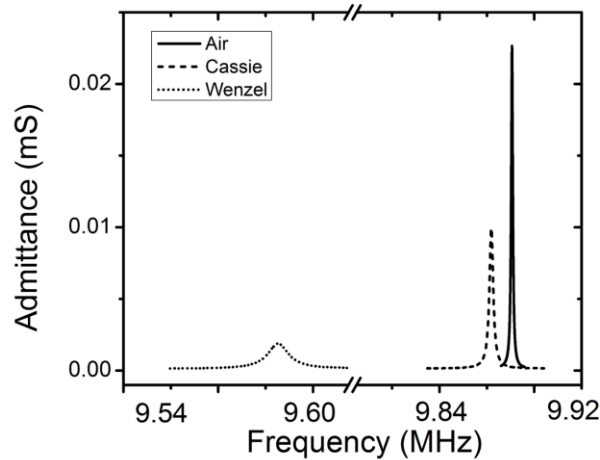


Figure S7. Frequency responses of micropillar-patterned QCM with a pillar height of 24  $\mu\text{m}$ .

#### S5. The energy barrier for the transient of wetting states

For a droplet on the pillar-based microstructures, the total interfacial energy of contact area beneath the droplet can be evaluated by summing up the interfacial energy. For a droplet in the Cassie state, the interfacial energy per unit area is given as

$$E_C = f\gamma_{SL} + (1 - f)\gamma_{LV} + (1 - f + \frac{\pi DH}{s^2})\gamma_{SV} \quad (\text{S-12})$$

For the Wenzel state:

$$E_W = \left(1 + \frac{\pi DH}{S^2}\right) \gamma_{SL} \quad (S-13)$$

The energy difference between the Cassie and Wenzel states is

$$E_C - E_W = \left(1 - f + \frac{\pi DH}{S^2}\right) \gamma_{LV} \cos \theta_0 + (1 - f) \gamma_{LV} \quad (S-14)$$

The Cassie state possesses a higher energy than the Wenzel state, i.e.,  $(E_C - E_W) > 0$ , and the liquid can instantaneously penetrate the cavities, resulting in a transition from the Cassie to the Wenzel state. However, external energy is required to overcome the energy barrier for this transition process. The energy barrier is due to the replacement of solid/vapor interface with solid/liquid interface when  $\gamma_{SL} > \gamma_{SV}$ .

The interfacial energy for a liquid with a penetration depth ( $y$ ) is

$$E_y = \left(f + \frac{\pi Dy}{S^2}\right) \gamma_{SL} + (1 - f) \gamma_{LV} + \left(1 - f + \frac{\pi D(H-y)}{S^2}\right) \gamma_{SV} \quad (S-15)$$

The energy barrier is obtained from (S-12) and (S-15)

$$\Delta E_y = E_y - E_C = \frac{\pi Dy}{S^2} (\gamma_{SL} - \gamma_{SV}) \quad (S-16)$$

For pillars with a height  $H$

$$\Delta E_H = \frac{\pi DH}{S^2} (\gamma_{SL} - \gamma_{SV}) \quad (S-17)$$

This indicates that the energy barrier is a function of side wall area per unit area ( $\pi DH/S^2$ ), and the interfacial energy difference between the solid/liquid and solid/vapor interfaces ( $\gamma_{SL} - \gamma_{SV}$ ).

In this research, the PMMA surfaces were hydrophobized with a PFOTS coating, and the interfacial energy is related to the concentration of  $-\text{CF}_2$  and  $-\text{CF}_3$  groups on this surface. For a surface with high concentration  $-\text{CF}_3$ ,  $\gamma_{SV} = 18.0 \text{ mN/m}$ .<sup>6</sup> Considering the measured contact angle for PFOTS-coated flat PMMA films ( $107.3 \pm 0.6^\circ$ ), and the interfacial energy of liquid/vapor for water  $\gamma_{LV} = \sigma = 73.0 \text{ mN/m}$ , the interfacial energy of solid/liquid can be determined with Young's equation, as  $\gamma_{SL} = 39.4 \text{ mN/m}$ .

The interfacial energies for the transition from the Cassie to the Wenzel state on pillar-based microstructures are illustrated in Figure S8. The Cassie state is meta-stable with  $E_C = 110.9 \text{ mN/m}$ , while the Wenzel state is stable with a lower interfacial energy  $E_W = 97.5 \text{ mN/m}$ . In the transition process, liquid penetrated vertically into the cavities, and the interfacial energy  $E_y$  increased linearly with the penetration depth, resulting in an energy barrier  $\Delta E_H = 31.6 \text{ mN/m}$ .

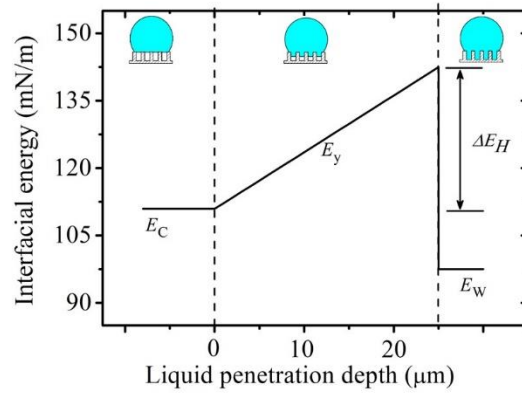


Figure S8. Energy barrier for the Cassie and Wenzel states. (pillar height =  $24 \mu\text{m}$ )

### S6. The transition from the Cassie state to the Wenzel state

The movement of the liquid-air interface during the transition process was depicted in Figure S9. The initial contact angle is  $91.3^\circ$ , as described as Eq. (S-11). When an external perturbation is applied such as vibration or pressure on the droplet, the contact angle increases due to the increase of the Laplace pressure, leading to an increased curvature of the liquid-air interface under the water droplet. The meniscus/interface reaches its minimum radius or maximum pendant depth ( $\delta_{\text{max}}$ ), while the contact angle reaches the critical value for advancing (advancing contact angle,  $\theta_{\text{adv}} = 117^\circ$ ). Then the liquid-air interface moves downward while keeping the advanced contact angles.

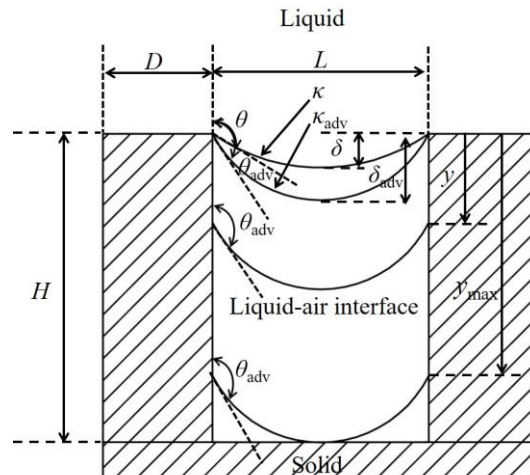


Figure S9. Schematic of the propagation of the liquid-air interface during the transition from Cassie to Wenzel state.

#### References:

1. Jokinen, V.; Suvanto, P.; Franssila, S. Oxygen and nitrogen plasma hydrophilization and hydrophobic recovery of polymers. *Biomicrofluidics* **2012**, *6* (1), 016501-016501-10.
2. Rykaczewski, K.; Landin, T.; Walker, M. L.; Scott, J. H. J.; Varanasi, K. K. Direct Imaging of Complex Nano- to Microscale Interfaces Involving Solid, Liquid, and Gas Phases. *ACS Nano* **2012**, *6* (10), 9326-9334.
3. Zhu, Y.; Antao, D. S.; Lu, Z.; Somasundaram, S.; Zhang, T.; Wang, E. N. Prediction and Characterization of Dry-out Heat Flux in Micropillar Wick Structures. *Langmuir* **2016**, *32* (7), 1920-1927.
4. Ibrahim, E. A.; Yang, H. Q.; Przekwas, A. J. Modeling of spray droplets deformation and breakup. *J. Propul. Power* **1993**, *9* (4), 651-654.
5. Haimov, B.; Pechook, S.; Ternyak, O.; Pokroy, B. Shape of Water–Air Interface beneath a Drop on a Superhydrophobic Surface Revealed: Constant Curvature That Approaches Zero. *The J. Phys. Chem. C* **2013**, *117* (13), 6658-6663.
6. Aulin, C.; Yun, S. H.; Wågberg, L.; Lindström, T. Design of Highly Oleophobic Cellulose Surfaces from Structured Silicon Templates. *ACS Appl. Mater. Interfaces* **2009**, *1* (11), 2443-2452.